Local Excitations of a Charged Nitrogen Vacancy in Diamond with Multireference Density Matrix Embedding Theory

Soumi Haldar,[†] Abhishek Mitra,[†] Matthew R. Hermes,[†] and Laura Gagliardi[*,‡,¶]

[†]*Department of Chemistry, Chicago Center for Theoretical Chemistry, University of Chicago, Chicago, IL 60637, USA.*

[‡]*Department of Chemistry, Pritzker School of Molecular Engineering, James Franck Institute, Chicago Center for Theoretical Chemistry, University of Chicago, Chicago, IL 60637, USA.*

[¶]*Argonne National Laboratory 9700 S. Cass Avenue Lemont, IL 60439*

E-mail: lgagliardi@uchicago.edu

Abstract

We investigate the negatively charged nitrogen-vacancy center in diamond using periodic density matrix embedding theory (pDMET). To describe the strongly correlated excited states of this system, the complete active space self-consistent field (CASSCF) followed by n-electron valence state second-order perturbation theory (NEVPT2) was used as impurity solver. Since the NEVPT2-DMET energies show a linear dependence on the inverse of the size of the embedding subspace, we performed an extrapolation of the excitation energies to the non-embedding limit using linear regression. The extrapolated NEVPT2-DMET first triplet-triplet excitation energy is 2.31 eV and that for the optically inactive singlet-singlet transition is 1.02 eV, both in agreement with the experimentally observed vertical excitation energies of ∼2.18 eV and ∼1.26 eV,

respectively. This is the first application of pDMET to a charged periodic system and the first investigation of the NV^- defect using NEVPT2 for periodic supercell models.

A naturally occuring diamond impurity is formed when a carbon atom is replaced with a nitrogen and another neighbouring carbon atom is missing from the lattice site. Together the nitrogen and the vacancy act as a single entity - the NV center in diamond.[1,2] The vacancy site of the neutral NV center can trap an extra electron from neighbouring isolated substitutional nitrogen defects, resulting in a charge-negative state (NV^- defect). This point defect introduces electronic levels within the fundamental band gap of diamond giving rise to interesting optical and magnetic properties not observed in pure diamond.[3,4] Most importantly, the characteristic ground and excited electronic spin states in the NV^- center make it stand out as one of the most promising solid-state spin qubits in the field of quantum information technology.[5–8] The electron spin qubit can be efficiently initialized, manipulated, and read out through an optical spin-polarization cycle involving the triplet ground state and the first triplet excited state via two intermediate spin singlets.[9–12] Moreover, it exhibits a long spin coherence time of a milli-second,[13] that persists even at room temperature, which means it can be efficiently used to store quantum information. Additionally, the NV^- electron spin can coherently couple with the neighbouring ^{13}C nuclear spin allowing to create a controllable few-qubit quantum register.[14,15]

To understand the NV^- center in diamond, accurate first principles simulations of its ground and excited states are important. Among different quantum chemical methods, density functional theory (DFT) has most widely been used to study this system[4,16–21] owing to its simplicity and computational affordability. However, DFT is not always accurate enough to describe solid-state spin defects with multireference character originating from the strongly correlated excited states that cannot be approximated by a single Slater determinant. The alternative approaches beyond DFT employed for the NV^- center include many-body perturbation theory - a combination of GW approximation[22] and Bethe Salpeter equation,[23] and configuration interaction constrained random phase approximation (CI-CRPA).[24]

Traditional multireference methods such as the complete active space self consistent field (CASSCF)[25–27] and multireference configuration interaction (MRCI)[26] have also been tested on molecular cluster models of the NV^- center. However, finite-size models do not include bulk long-range effects, and they may introduce spurious boundary effects. Furthermore, defect excitation energies, especially those involving higher energy states, are highly sensitive to the shape and size of the cluster.[25,27] On the other hand, for supercell models based on periodic boundary conditions, that are generally more appropriate to describe such solid state systems, direct application of multireference methods is often unfeasible due to their high computational cost. As a middle ground, quantum embedding theories offer an attractive solution, providing a trade-off between computational cost and accuracy.

Quantum embedding allows one to divide a bulk problem into sub-problems such that a particular region of interest, known as the "active region" or "impurity", is treated with a more accurate and thus more expensive method, while the rest of the system is described using a mean-field approach. There are many different versions of quantum embedding techniques,[28,29] which are classified based on the level of theory used to analyze the sub problems and the key quantum variable used to connect the high- and low-level methods. Notably, quantum embedding methods where DFT is used as the lower level theory suffer from an inherent "double counting" issue. This problem refers to the incomplete cancellation of the terms that are computed both in DFT and in the high level theory employed for the active region. Recently Galli et al.[30] proposed an exact double counting correction scheme to their quantum defect embedding theory (QDET), based on a Green's function formulation. They applied this method to study the electronic structure and energy spacings in the NV^- center and achieved excellent agreement with experiments, which was not possible using their original QDET implementation based on an approximate double counting correction.[30]

A different flavour of quantum embedding is density matrix embedding theory[31] (DMET). The key quantum variable in DMET is the frequency-independent one-body reduced density matrix that makes it much simpler and computationally less expensive compared to frequency

dependent Green's function-based embedding methods[31] e.g. dynamical mean-field theory. It is a local impurity model where the Hilbert space dimension can be considerably reduced by projecting the original Hamiltonian onto a small impurity subspace. This method is able to capture the explicit quantum entanglement between the active region and its environment. In this work, we use a periodic version of DMET (pDMET)[32,33] to investigate the NV^- system. Unlike QDET, we use restricted open-shell Hartree-Fock (ROHF) as the lower level theory, which makes the method free from the "double counting" problem. We use CASSCF[34–36] as the high-level impurity solver to appropriately address the strongly correlated defect region, followed by n-electron valence state second-order perturbation theory (NEVPT2),[37–40] to account for the portion of dynamic correlation which is missing at the CASSCF level. The rest of the system (environment) is approximately described with a "bath" constructed from a Schmidt decomposition[41] of the full-system HF wave function. Recently, it has been shown that pDMET offers an accurate and affordable *ab initio* approach for studying the electronic structure of neutral point defects.[42,43] However, pDMET has not yet been investigated for charged defects. In this work, we focus on the well tested NV^- center in diamond to explore the performance of pDMET for charged electronic excitations localized within the defect site. To our knowledge, this is the first investigation of the NV^- defect using CASSCF/NEVPT2 for periodic supercell models.

The photoluminescence band of the NV^- center in diamond shows a strong optical transition with a sharp zero phonon line (ZPL) at 1.945 eV (637 nm) along with a phonon side band in the absorption spectra with maximum intensity peak at $\sim$2.18 eV.[44] Davies and Hamer analyzed this experimental ZPL and found that the defect center has a trigonal C_{3V} symmetry and the ZPL is associated with a strong optical transition between the triplet ground state $^3A_2$ and the first excited triplet state ^3E.[44] The defect center also exhibits a weak band in the infrared region with a ZPL at 1.19 eV (1046 nm)[45] along with a phonon side band with maximum intensity peak at 1.26 eV[46] in the absorption spectra. This ZPL corresponds to a transition between two intermediate metastable singlet states - $^1A_1$ and ^1E located between

the two triplets. The optical transition involving the $m_s = 0$ sublevels of the ground and

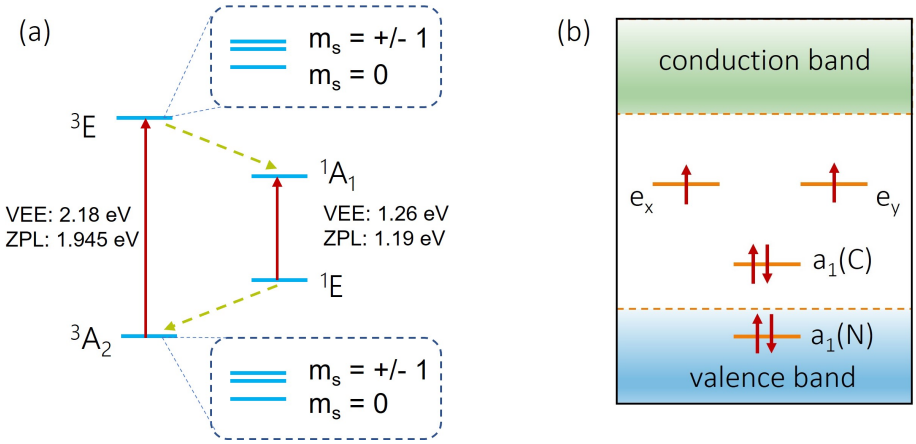

Figure 1: (a) Many-body electronic states and the electronic transitions in the NV$^-$ defect in diamond. The red arrows represent electronic excitations and the green dashed arrows represent the intersystem crossing process. (b) Ground state electronic configuration (energy levels are qualitative only) of the NV$^-$ center.

excited triplet states is spin conserving and therefore the final state after deexcitation is the $m_s = 0$ sublevel of the ground state. However, the excitation involving the $m_s = \pm 1$ levels follows an intersystem crossing path via the intermediate singlet states and finally decays to the $m_s = 0$ sublevel of the ground state.[12,47] The intermediate singlets thus play a crucial role in the optical initialization of defect spin state through the spin polarization process. The schematic electronic energy level diagram and the spin polarization process in the NV$^-$ defect is shown in Fig. 1a. In this work, we use the ground state ($^3A_2$) geometry and compute the energies corresponding to the triplet-triplet ($^3A_2 \rightarrow {}^3E$), singlet-singlet ($^1E \rightarrow {}^1A_1$) and the triplet-singlet ($^3A_2 \rightarrow {}^1E$ and $^3A_2 \rightarrow {}^1A_1$) vertical excitations.

The ground state of the $^3A_2$ triplet, belonging to the C_{3v} point group, is characterized by a doubly occupied a_1 orbital and singly occupied e_x and e_y orbitals, leading to the configuration $a_1^2 e_x^1 e_y^1$. Our ROHF calculation confirms this. Another a_1 orbital is present at a lower energy within the valence band. The ground state configuration of the NV$^-$ center is shown in Fig. 1b.

We considered three different supercells of increasing size - NC_{62}, NC_{126}, and NC_{214}. NC_{62} and NC_{214} are the 2x2x2 and 3x3x3 supercells constructed from an 8-atom unit cell, whereas

NC_{126} is the 4x4x4 supercell constructed from a 2-atom unit cell. All the structures of the different supercells were optimized with the VASP code,[48,49] using plane wave basis set (with an energy cutoff of 500 eV) with the PBESol functional[50] which is particularly suitable for solids. We used spin polarization and no symmetry restriction. The bond distances in the optimized geometry are consistent with those reported in the literature[25,51] from other DFT optimizations. The N-C bond lengths in the optimized structure is 1.46 Å. The distance between the N atom and the 3 C atoms forming the dangling bonds with the vacancy is 2.72 Å. The distance between any two C atoms among the 3 C atoms forming the dangling bonds is 2.64 Å. We confirmed that the geometries do not change significantly for 3 different supercells. Along with the supercell models we also used a finite molecular cluster model $C_{33}H_{36}N^{-}$. The method and model used for the cluster calculations are reported in the Supporting Information (SI).

For the detailed theoretical foundation of pDMET we refer to the literature 52 and 53. The pDMET algorithm starts with a mean-field calculation on the full system, in this case we used the periodic ROHF method. Since the translational symmetry is lost in the defective solid and we use sufficiently large supercells to model the defect, the Brillouin zone is sampled only at the Γ- point.

The canonical HF molecular orbitals initially delocalized over the whole system, are localized to define a local fragment and its environment, using the maximally localized Wannier functions (MLWFs)[54,55] obtained from the mean-field orbitals using wannier90[56] code via the pyWannier90 interface.[57] After the orbital localization, choosing a physically motivated impurity cluster is a key step in DMET calculations. The impurity cluster is defined by a set of atoms on which the MLWFs are spatially localized. Since we are interested in the defect-localized transitions, a reasonable choice of the impurity cluster would be the one that includes the atoms comprising and surrounding the defect center. We consider a 16 atom impurity cluster (NC_{15}) that includes the N atom and the C atoms closest to the N and the vacancy site. In Fig. 2, all 3 supercells considered are shown along with the atoms within

the impurity cluster specifically highlighted.

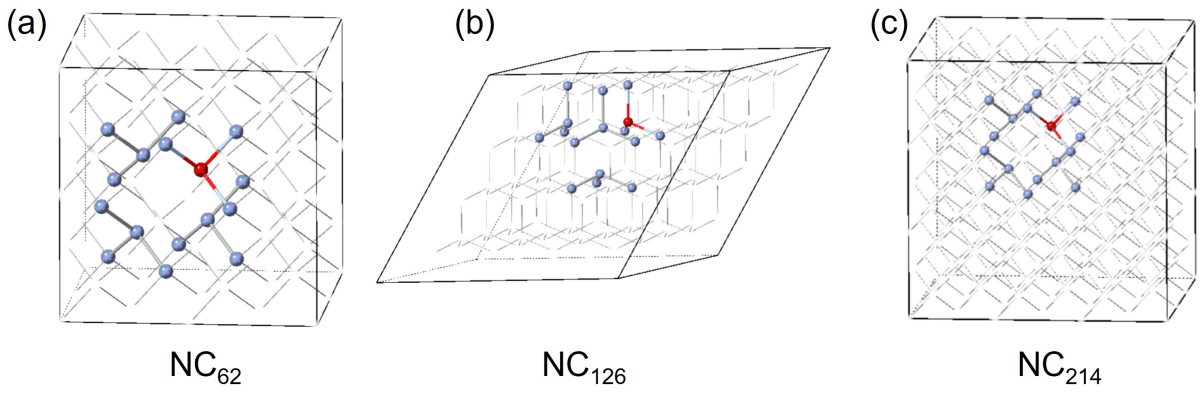

Figure 2: Three supercell models: NC_{62}, NC_{126}, and NC_{214} for NV^- defect in diamond. In each of them the NC_{15} impurity cluster for the DMET calculations has been highlighted.

The environment of the impurity cluster is approximately represented by a set of bath orbitals (constructed using a Schmidt decomposition[58] of the ROHF wave function) that are most entangled with the fragment orbitals in the impurity cluster. The original Hamiltonian is then projected onto the combined space of fragment and bath orbitals and the high-level wave function is determined using CASSCF, followed by NEVPT2 for the energy calculation. The CAS-DMET (using CASSCF as the impurity solver) and NEVPT2-DMET (using NEVPT2 as the impurity solver) calculations were performed using the pDMET code,[59,60] and the PySCF package[61,62] to obtain the electron integrals and for the quantum chemical solvers. For both molecular CASSCF/NEVPT2 and periodic CAS-DMET/NEVPT2-DMET calculations an active space containing 10 electrons in 9 orbitals (10e, 9o) was employed. This includes symmetry-adapted orbitals that are consistently obtainable across all the different supercell sizes as well as for the finite molecular cluster model. The detailed analysis of the active space convergence is presented in the SI. Further, the triplet excitation involves the non-degenerate ground state triplet $^3A_2$ and the doubly degenerate ^3E state, whereas the optically inactive singlet transition takes place from the doubly degenerate ^1E to the non-degenerate $^1A_1$ state. We therefore considered two separate state-average CASSCF (SA-CASSCF) calculations, one on the three lowest-energy triplets, and one on the three

lowest-energy singlets. In both calculations equal weight in the state average was attributed to all states. The triplet-singlet energy gaps ($^3A_2 \rightarrow ^1E$ and $^3A_2 \rightarrow ^1A_1$) were computed from the difference between the state-averaged singlet and the state-averaged triplet calculations. We used GTH pseudopotentials[63] to replace the core electron density. For the valence electrons, we used the GTH basis set of triple zeta (gth-tzvp) quality for the N and six C atoms - three attached to the N, and the other three making dangling bonds with the vacancy, and of double zeta (gth-dzv) quality for the remaining atoms. This combination of basis sets (gth-dzv + gth-tzvp) was employed for all the calculations described in this work, if not mentioned otherwise.

In Fig. 3 we show the (10e, 9o) active orbitals along with their natural occupancies for the smallest supercell NC_{62}. Similar orbitals and occupancies were obtained for the larger supercells NC_{126} and NC_{214}, and the cluster (shown in SI).

We analyzed the impact of the size of the DMET embedding subspace on the computed vertical excitation energies (VEE) for three supercells. To do this, we used a 16-atom impurity cluster (NC_{15}) and performed the CAS-DMET/NEVPT2-DMET calculations using different numbers of fragment + bath orbitals. A comprehensive explanation of the procedure in which this was accomplished can be found in the SI. The individual VEEs corresponding to different numbers of embedding orbitals are also reported in the SI.

In all cases the CAS-DMET VEEs remain almost unaffected by the embedding size. On the other hand, the NEVPT2-DMET VEEs decrease as the size of the embedding space increases. We observe a linear dependence of the NEVPT2-DMET VEE on the inverse of the number of embedding orbitals. This motivated us to perform a linear extrapolation to achieve the non-embedding limit. For a supercell as small as NC_{62}, it is possible to perform a full non-embedding calculation, while for larger supercells this is not affordable, and this is why an embedding technique is needed in the first place. Therefore, such a linear extrapolation is necessary to achieve the non-embedding limit of the NEVPT2-DMET excitation energy.

Moreover, for any embedding size, CASSCF significantly overestimates the VEEs as com-

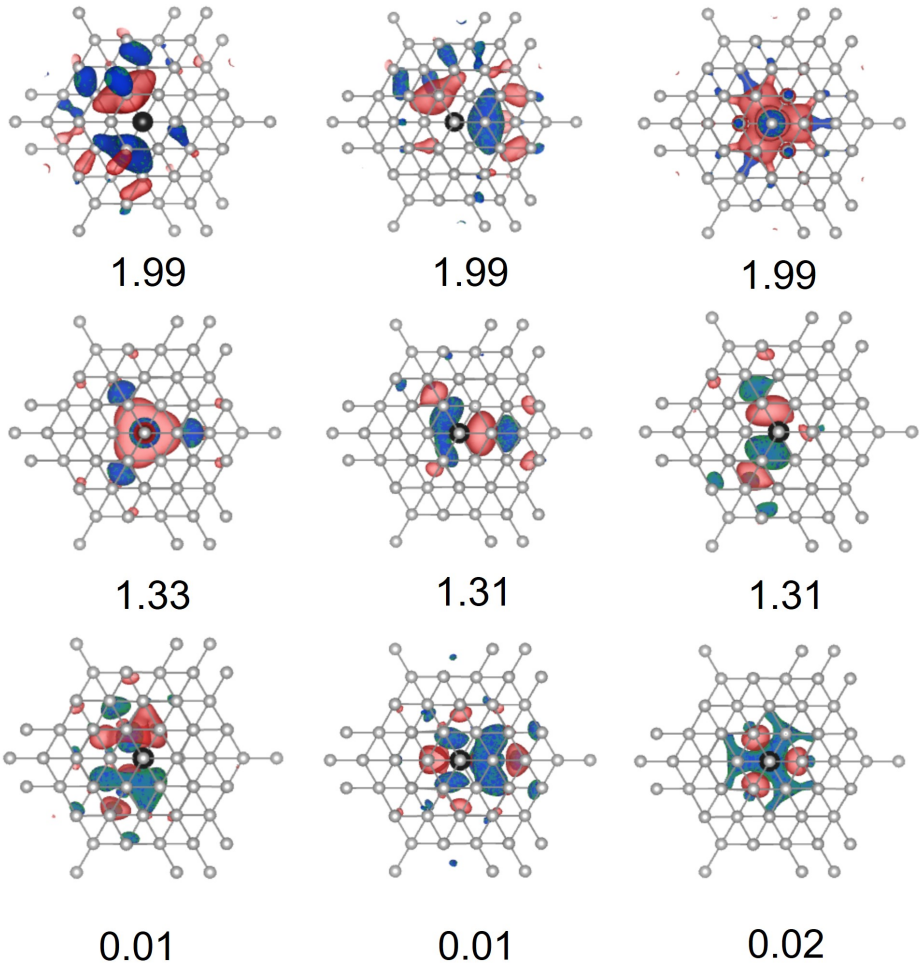

Figure 3: (10e, 9o) active orbitals for NC_{62} supercell with an isosurface value of 0.04. Natural occupancies are mentioned below.

pared to the experimental data. NEVPT2 corrects the CASSCF VEEs by almost one eV, highlighting the importance of dynamic correlation effects. A similar conclusion was drawn by Zyubin et al.[26] where reasonable agreement of calculated transition energies with experiment was achieved only at the CASPT2[64] level.

Furthermore, for specific embedding sizes, convergence in the VEEs is observed as the supercell size becomes sufficiently large. E.g., using 484 (fragment + bath) orbitals the NEVPT2-DMET $^3A_2 \rightarrow {}^3E$ VEE increases by 0.34 eV going from NC_{62} to NC_{126}, whereas it increases only by 0.03 eV from NC_{126} to NC_{214}. Similar energy differences are observed for the singlet excitation as well. Going from NC_{62} to NC_{126} the difference is 0.43 eV, whereas it decreases

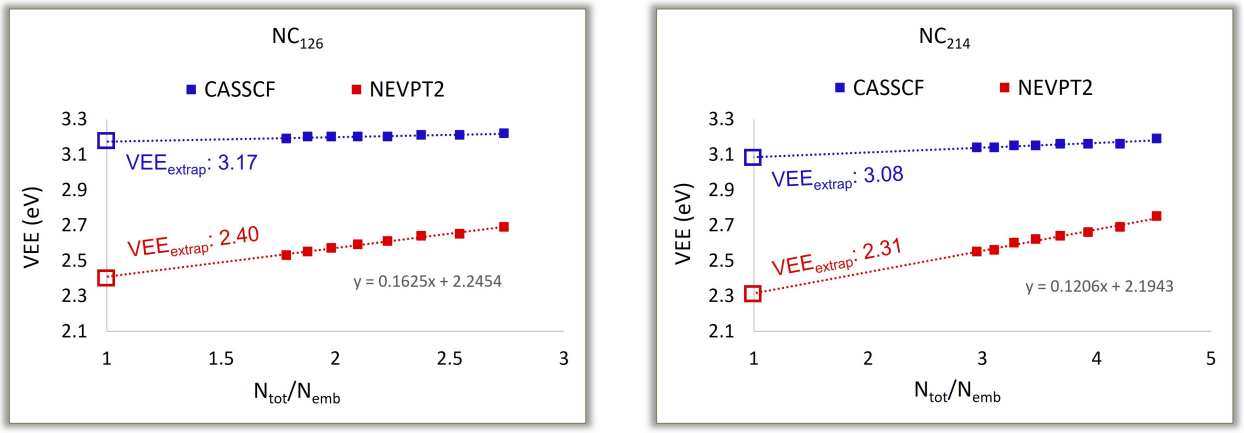

Figure 4: CAS-DMET and NEVPT2-DMET excitation energies for ${}^3A_2 \rightarrow {}^3E$ transition and their extrapolation to the non-embedding limit for NC_{126} and NC_{214}. N_{tot} represents the total number of MLWFs in the respective supercells and N_{emb} is the number of MLWFs within the embedding subspace. $N_{emb} = N_{frag} + N_{bath}$. The hollow sqaures represent the extrapolated VEE values.

to only 0.02 eV from NC_{126} to NC_{214}. The triplet-singlet energy gaps also follow a similar convergence trend. We therefore performed the linear extrapolation only for the two larger supercells - NC_{126} and NC_{214}.

In Fig. 4 we plot the ${}^3A_2 \rightarrow {}^3E$ VEEs as a function of a ratio of the total number of MLWFs (N_{tot}) in the cell to the number of orbitals (fragment + bath) in the embedding subspace (N_{emb}). Upon extrapolation, the NEVPT2-DMET VEE attains a value of 2.40 eV for NC_{126} and 2.31 eV for NC_{214} when extrapolated to the non-embedding limit (at $N_{tot}/N_{emb} = 1$). The extrapolated ${}^3A_2 \rightarrow {}^3E$ VEE for the largest supercell NC_{214} is within 0.13 eV of the reference experimental VEE of ∼2.18 eV. Clearly, the linear extrapolation of the NEVPT2-DMET VEEs provides quantitative agreement with experiment, bypassing the expensive non-embedding calculations for large supercell models. Extrapolation plots for the other excitations are shown in the SI.

In Table 1 we report the VEEs of the ${}^3E$, ${}^1E$, and ${}^1A_1$ states with respect to the ground state (${}^3A_2$) as well as the ${}^1E \rightarrow {}^1A_1$ VEE, and compare our extrapolated values with the experimental VEEs that correspond to the maximum intensity peaks of the phonon side bands in the experimental absorption spectra. For completeness, the ZPL values have also

been included in the table. Notably, the "experimental" ZPLs/VEEs (marked with *) of the $^3A_2 \rightarrow {}^1E$ and $^3A_2 \rightarrow {}^1A_1$ are not directly measured from experiments. Those are derived from the experimental ZPLs/VEEs of the $^3A_2 \rightarrow {}^3E$ (1.945/2.18 eV) and $^1A_1 \rightarrow {}^1E$ (1.19/1.26 eV) transitions, and the energy difference between the ^3E and $^1A_1$ states (0.321-0.414 eV).[65]

Table 1: **NEVPT2-DMET (extraploted) VEEs (eV) for the NC_{126} and NC_{214} supercells compared with experimental and previous theoretical values.**

Reference/Electronic state	$^3A_2 \rightarrow {}^1E$	$^3A_2 \rightarrow {}^1A_1$	$^3A_2 \rightarrow {}^3E$	^1E to $^1A_1$
Exp. VEE	0.50-0.59*	1.76-1.85*	∼2.18[44]	∼1.26[46]
Exp. ZPL	0.34-0.43*	1.51-1.60*	1.945[44]	1.19[45]
NC_{214} supercell (This work)	0.50	1.56	2.31	1.02
NC_{126} supercell (This work)	0.53	1.62	2.40	1.07
DFT-LSDA 512 atom supercell[51]			1.91	
DFT-PBE 256 atom supercell[23]			1.87	
GW+BSE 256 atom supercell[23]	0.40	0.99	2.32	
Model fit from GW+CI[10]	0.50	1.50	2.1	
Model from CRPA + CI[24]	0.49	1.41	2.02	
$C_{19}H_{28}N^-$ CASSCF(8,11)[26]	0.44	1.00	0.98	
$C_{19}H_{28}N^-$ MRCI(8,10)[26]	0.50	1.23	1.36	
$C_{49}H_{52}N^-$ cluster CASSCF(6,8)[27]			2.57	
$C_{33}H_{36}N^-$ cluster CASSCF(6,8)[27]			2.48	
$C_{85}H_{76}N^-$ cluster CASSCF(6,6)[25]	0.25	1.60	2.14	1.35
$C_{33}H_{36}N^-$ cluster CASSCF(6,6)[25]	0.34	1.41	1.93	1.07
NC_{510} supercell QDET (EDC@G_0W_0)[30]	0.463	1.270	2.152	
NC_{510} supercell QDET (HFDC)[30]	0.375	1.150	1.324	

Although the DFT calculations can accurately predict the triplet energies, the singlet energies and their ordering largely varies for different DFT calculations.[66] Gali et al.[51] reported a $^3A_2 \rightarrow {}^3E$ VEE value of 1.91 eV (using the local spin density approximation (LSDA) and a 512 atom supercell). They predicted an energy ordering of the metastable singlet states $^1A_1 < {}^1E$, which is opposite to our prediction. Rogers et al.[45] measured a ZPL of 1046 nm and assigned it to the $^1A_1 \leftrightarrow {}^1E$ transition, although the ordering was not conclusive. In a subsequent study Gali et al.[23] reported a $^3A_2 \rightarrow {}^3E$ VEE of 1.87 eV (DFT-PBE with a 256 atom supercell) and a GW+BSE value of 2.32 eV, (in agreement with our extrapolated

VEE of 2.31 eV for the 215 atom supercell), with a reversed relative ordering, consistent with a subsequent pump-probe spectroscopy measurement.[46] Among other beyond-DFT treatments, the GW+CI (2.1 eV)[10] and CI-CRPA (2.02 eV)[24] VEEs are close to our results. For molecular CASSCF and MRCI calculations, different active spaces (AS) and different finite size model clusters have been used. The $^3A_2 \rightarrow {}^3E$ VEE ranges from 0.98 eV on a $C_{19}H_{28}N^-$ cluster, AS(8e, 11o)[26] to 2.57 eV on a $C_{49}H_{52}N^-$ cluster, AS(6e, 8o).[27] Moreover, different VEEs have been obtained using the same level of theory and basis set, but different cluster models.[25,27] The finite size of the clusters may not be large enough to reproduce bulk effects and the spurious surface hydrogens may also alter the electronic distribution in the system, as discussed by Park and co-workers.[25] They calculated a triplet VEE of 2.14 eV, in agreement with the experimental VEE ($\sim$2.18 eV) using a large enough cluster model $C_{85}H_{76}N^-$.

Finally, Galli et al.[30] predicted a $^3A_2 \rightarrow {}^3E$ VEE of 2.152 eV using quantum defect embedding theory (QDET) with an exact double-counting (DC) correction, while they reported a value of 1.324 eV using an approximate DC correction. DC occurs in DFT-based embedding methods, while our pDMET formulation does not have this issue because HF is used as low-level theory.

In summary, we employed a wave function in wave function embedding method to compute the electronic excitations of the NV^- defect in diamond. This is the first time pDMET was employed for a charged species and the first investigation of the NV^- defect using CASSCF/NEVPT2 for periodic supercell models. Compared to hydrogenated molecular cluster models, our calculations with periodic boundary conditions provide a more realistic description of the localized crystal defect. We observed a linear dependence of the NEVPT2-DMET energies on the inverse of the size of the embedding subspace and thus extrapolated to the non-embedding limit. The extrapolated triplet-triplet and singlet-singlet energy gaps for the large supercell are 0.1-0.2 eV within the experimental values. The vertical energy gaps of the singlet states with respect to the triplet ground state are also consistent with

previous theoretical studies. We envision that extrapolations based on pDMET calculations can be used routinely in the future to study strongly correlated charged point defects in solids.

Acknowledgement

M.R.H. and L.G. are partially supported by the U.S. Department of Energy (DOE), Office of Basic Energy Sciences, Division of Chemical Sciences, Geosciences, and Biosciences under grant no. USDOE/DE-SC002183. This material is based upon work supported by the U.S. Department of Energy, Office of Science, National Quantum Information Science Research Centers. We acknowledge the Research Computing Center (RCC) at the University of Chicago for access to computing resources.

Supporting Information Available

The finite cluster model, active space convergence, procedure to vary the size of embedding subspace, excitation energies using different numbers of embedding orbitals, extrapolation to the non-embedding limit, total energies and results with different basis sets.

References

(1) Gruber, A.; Dräbenstedt, A.; Tietz, C.; Fleury, L.; Wrachtrup, J.; von Borczyskowski, C. Scanning Confocal Optical Microscopy and Magnetic Resonance on Single Defect Centers. *Science* **1997**, *276*, 2012–2014.

(2) Dräbenstedt, A.; Fleury, L.; Tietz, C.; Jelezko, F.; Kilin, S.; Nizovtzev, A.; Wrachtrup, J. Low-temperature microscopy and spectroscopy on single defect centers in diamond. *Phys. Rev. B* **1999**, *60*, 11503–11508.

(3) Jin, Y.; Govoni, M.; Galli, G. Vibrationally resolved optical excitations of the nitrogen-vacancy center in diamond. *npj Computational Materials* **2022**, *8*, 1–9.

(4) Ádám Gali, Ab initio theory of the nitrogen-vacancy center in diamond. *Nanophotonics* **2019**, *8*, 1907–1943.

(5) Wrachtrup, J.; Kilin, S. Y.; Nizovtsev, A. Quantum computation using the 13C nuclear spins near the single NV defect center in diamond. *Optics and Spectroscopy* **2001**, *91*, 429–437.

(6) Jelezko, F.; Popa, I.; Gruber, A.; Tietz, C.; Wrachtrup, J.; Nizovtsev, A.; Kilin, S. Single spin states in a defect center resolved by optical spectroscopy. *Applied Physics Letters* **2002**, *81*, 2160–2162.

(7) Jelezko, F.; Gaebel, T.; Popa, I.; Gruber, A.; Wrachtrup, J. Observation of Coherent Oscillations in a Single Electron Spin. *Phys. Rev. Lett.* **2004**, *92*, 076401.

(8) Jelezko, F.; Gaebel, T.; Popa, I.; Domhan, M.; Gruber, A.; Wrachtrup, J. Observation of Coherent Oscillation of a Single Nuclear Spin and Realization of a Two-Qubit Conditional Quantum Gate. *Phys. Rev. Lett.* **2004**, *93*, 130501.

(9) Robledo, L.; Bernien, H.; van der Sar, T.; Hanson, R. Spin dynamics in the optical cycle of single nitrogen-vacancy centres in diamond. *New Journal of Physics* **2011**, *13*, 025013.

(10) Choi, S.; Jain, M.; Louie, S. G. Mechanism for optical initialization of spin in NV^- center in diamond. *Phys. Rev. B* **2012**, *86*, 041202.

(11) Goldman, M. L.; Doherty, M. W.; Sipahigil, A.; Yao, N. Y.; Bennett, S. D.; Manson, N. B.; Kubanek, A.; Lukin, M. D. State-selective intersystem crossing in nitrogen-vacancy centers. *Phys. Rev. B* **2015**, *91*, 165201.

(12) Thiering, G. m. H.; Gali, A. Theory of the optical spin-polarization loop of the nitrogen-vacancy center in diamond. *Phys. Rev. B* **2018**, *98*, 085207.

(13) Balasubramanian, G.; Neumann, P.; Twitchen, D.; Markham, M.; Kolesov, R.; Mizuochi, N.; Isoya, J.; Achard, J.; Beck, J.; Tissler, J., et al. Ultralong spin coherence time in isotopically engineered diamond. *Nature materials* **2009**, *8*, 383–387.

(14) Childress, L.; Dutt, M. V. G.; Taylor, J. M.; Zibrov, A. S.; Jelezko, F.; Wrachtrup, J.; Hemmer, P. R.; Lukin, M. D. Coherent Dynamics of Coupled Electron and Nuclear Spin Qubits in Diamond. *Science* **2006**, *314*, 281–285.

(15) Dutt, M. V. G.; Childress, L.; Jiang, L.; Togan, E.; Maze, J.; Jelezko, F.; Zibrov, A. S.; Hemmer, P. R.; Lukin, M. D. Quantum Register Based on Individual Electronic and Nuclear Spin Qubits in Diamond. *Science* **2007**, *316*, 1312–1316.

(16) Gali, A.; Janzén, E.; Deák, P.; Kresse, G.; Kaxiras, E. Theory of Spin-Conserving Excitation of the $N - V^-$ Center in Diamond. *Phys. Rev. Lett.* **2009**, *103*, 186404.

(17) Gali, A. Time-dependent density functional study on the excitation spectrum of point defects in semiconductors. *physica status solidi (b)* **2011**, *248*, 1337–1346.

(18) Thiering, G. m. H.; Gali, A. Ab initio calculation of spin-orbit coupling for an NV center in diamond exhibiting dynamic Jahn-Teller effect. *Phys. Rev. B* **2017**, *96*, 081115.

(19) Alkauskas, A.; Buckley, B. B.; Awschalom, D. D.; de Walle, C. G. V. First-principles theory of the luminescence lineshape for the triplet transition in diamond NV centres. *New Journal of Physics* **2014**, *16*.

(20) Razinkovas, L.; Doherty, M. W.; Manson, N. B.; Van de Walle, C. G.; Alkauskas, A. Vibrational and vibronic structure of isolated point defects: The nitrogen-vacancy center in diamond. *Phys. Rev. B* **2021**, *104*, 045303.

(21) Jin, Y.; Govoni, M.; Wolfowicz, G.; Sullivan, S. E.; Heremans, F. J.; Awschalom, D. D.; Galli, G. Photoluminescence spectra of point defects in semiconductors: Validation of first-principles calculations. *Phys. Rev. Materials* **2021**, *5*, 084603.

(22) Onida, G.; Reining, L.; Rubio, A. Electronic excitations: density-functional versus many-body Green's-function approaches. *Rev. Mod. Phys.* **2002**, *74*, 601–659.

(23) Ma, Y.; Rohlfing, M.; Gali, A. Excited states of the negatively charged nitrogen-vacancy color center in diamond. *Phys. Rev. B* **2010**, *81*, 041204.

(24) Bockstedte, M.; Schütz, F.; Garratt, T.; Ivády, V.; Gali, A. Ab initio description of highly correlated states in defects for realizing quantum bits. *npj Quantum Materials* **2018**, *3*, 1–6.

(25) Bhandari, C.; Wysocki, A. L.; Economou, S. E.; Dev, P.; Park, K. Multiconfigurational study of the negatively charged nitrogen-vacancy center in diamond. *Phys. Rev. B* **2021**, *103*, 014115.

(26) Zyubin, A. S.; Mebel, A. M.; Hayashi, M.; Chang, H. C.; Lin, S. H. Quantum chemical modeling of photoadsorption properties of the nitrogen-vacancy point defect in diamond. *Journal of Computational Chemistry* **2009**, *30*, 119–131.

(27) Lin, C.-K.; Wang, Y.-H.; Chang, H.-C.; Hayashi, M.; Lin, S. H. One- and two-photon absorption properties of diamond nitrogen-vacancy defect centers: A theoretical study. *The Journal of Chemical Physics* **2008**, *129*, 124714.

(28) Sun, Q.; Chan, G. K.-L. Quantum Embedding Theories. *Accounts of Chemical Research* **2016**, *49*, 2705–2712.

(29) Vorwerk, C.; Sheng, N.; Govoni, M.; Huang, B.; Galli, G. Quantum embedding theories to simulate condensed systems on quantum computers. *Nature Computational Science* **2022**, *2*, 424–432.

(30) Sheng, N.; Vorwerk, C.; Govoni, M.; Galli, G. Green's Function Formulation of Quantum Defect Embedding Theory. *Journal of Chemical Theory and Computation* **2022**, *18*, 3512–3522.

(31) Knizia, G.; Chan, G. K.-L. Density Matrix Embedding: A Simple Alternative to Dynamical Mean-Field Theory. *Phys. Rev. Lett.* **2012**, *109*, 186404.

(32) Pham, H. Q.; Hermes, M. R.; Gagliardi, L. Periodic Electronic Structure Calculations with the Density Matrix Embedding Theory. *Journal of Chemical Theory and Computation* **2020**, *16*, 130–140.

(33) Cui, Z.-H.; Zhu, T.; Chan, G. K.-L. Efficient Implementation of Ab Initio Quantum Embedding in Periodic Systems: Density Matrix Embedding Theory. *Journal of Chemical Theory and Computation* **2020**, *16*, 119–129.

(34) Roos, B. O.; Taylor, P. R.; Sigbahn, P. E. A complete active space SCF method (CASSCF) using a density matrix formulated super-CI approach. *Chemical Physics* **1980**, *48*, 157–173.

(35) Siegbahn, P. E.; Almlöf, J.; Heiberg, A.; Roos, B. O. The complete active space SCF (CASSCF) method in a Newton–Raphson formulation with application to the HNO molecule. *The Journal of Chemical Physics* **1981**, *74*, 2384–2396.

(36) Siegbahn, P.; Heiberg, A.; Roos, B.; Levy, B. A comparison of the super-CI and the Newton-Raphson scheme in the complete active space SCF method. *Physica Scripta* **1980**, *21*, 323.

(37) Angeli, C.; Cimiraglia, R.; Evangelisti, S.; Leininger, T.; Malrieu, J.-P. Introduction of n-electron valence states for multireference perturbation theory. *The Journal of Chemical Physics* **2001**, *114*, 10252–10264.

(38) Angeli, C.; Borini, S.; Cestari, M.; Cimiraglia, R. A quasidegenerate formulation of the second order n-electron valence state perturbation theory approach. *The Journal of chemical physics* **2004**, *121*, 4043–4049.

(39) Angeli, C.; Cimiraglia, R.; Malrieu, J.-P. N-electron valence state perturbation theory: a fast implementation of the strongly contracted variant. *Chemical physics letters* **2001**, *350*, 297–305.

(40) Angeli, C.; Cimiraglia, R.; Malrieu, J.-P. n-electron valence state perturbation theory: A spinless formulation and an efficient implementation of the strongly contracted and of the partially contracted variants. *The Journal of chemical physics* **2002**, *117*, 9138–9153.

(41) Peschel, I.; Eisler, V. Reduced density matrices and entanglement entropy in free lattice models. *Journal of physics a: mathematical and theoretical* **2009**, *42*, 504003.

(42) Mitra, A.; Pham, H. Q.; Pandharkar, R.; Hermes, M. R.; Gagliardi, L. Excited States of Crystalline Point Defects with Multireference Density Matrix Embedding Theory. *The Journal of Physical Chemistry Letters* **2021**, *12*, 11688–11694.

(43) Mitra, A.; Hermes, M. R.; Cho, M.; Agarawal, V.; Gagliardi, L. Periodic Density Matrix Embedding for CO Adsorption on the MgO(001) Surface. *The Journal of Physical Chemistry Letters* **2022**, *13*, 7483–7489.

(44) Davies, G. J.; Hamer, M. F. Optical studies of the 1.945 eV vibronic band in diamond. *Proceedings of the Royal Society of London. A. Mathematical and Physical Sciences* **1976**, *348*, 285 – 298.

(45) Rogers, L.; Armstrong, S.; Sellars, M.; Manson, N. Infrared emission of the NV centre in diamond: Zeeman and uniaxial stress studies. *New Journal of Physics* **2008**, *10*, 103024.

(46) Kehayias, P.; Doherty, M. W.; English, D.; Fischer, R.; Jarmola, A.; Jensen, K.; Leefer, N.; Hemmer, P.; Manson, N. B.; Budker, D. Infrared absorption band and vibronic structure of the nitrogen-vacancy center in diamond. *Phys. Rev. B* **2013**, *88*, 165202.

(47) Koehl, W. F.; Seo, H.; Galli, G.; Awschalom, D. D. Designing defect spins for wafer-scale quantum technologies. *MRS Bulletin* **2015**, *40*, 1146–1153.

(48) Kresse, G.; Furthmüller, J. Efficient iterative schemes for ab initio total-energy calculations using a plane-wave basis set. *Phys. Rev. B* **1996**, *54*, 11169–11186.

(49) Kresse, G.; Furthmüller, J. Efficiency of ab-initio total energy calculations for metals and semiconductors using a plane-wave basis set. *Computational materials science* **1996**, *6*, 15–50.

(50) Perdew, J. P.; Ruzsinszky, A.; Csonka, G. I.; Vydrov, O. A.; Scuseria, G. E.; Constantin, L. A.; Zhou, X.; Burke, K. Restoring the Density-Gradient Expansion for Exchange in Solids and Surfaces. *Phys. Rev. Lett.* **2008**, *100*, 136406.

(51) Gali, A.; Fyta, M.; Kaxiras, E. Ab initio supercell calculations on nitrogen-vacancy center in diamond: Electronic structure and hyperfine tensors. *Physical Review B* **2008**, *77*, 155206.

(52) Cui, Z.-H.; Zhu, T.; Chan, G. K.-L. Efficient implementation of ab initio quantum embedding in periodic systems: Density matrix embedding theory. *Journal of Chemical Theory and Computation* **2019**, *16*, 119–129.

(53) Pham, H. Q.; Hermes, M. R.; Gagliardi, L. Periodic electronic structure calculations with the density matrix embedding theory. *Journal of Chemical Theory and Computation* **2019**, *16*, 130–140.

(54) Marzari, N.; Vanderbilt, D. Maximally localized generalized Wannier functions for composite energy bands. *Phys. Rev. B* **1997**, *56*, 12847–12865.

(55) Marzari, N.; Mostofi, A. A.; Yates, J. R.; Souza, I.; Vanderbilt, D. Maximally localized Wannier functions: Theory and applications. *Rev. Mod. Phys.* **2012**, *84*, 1419–1475.

(56) Pizzi, G. et al. Wannier90 as a community code: new features and applications. *Journal of Physics: Condensed Matter* **2020**, *32*, 165902.

(57) Pham, H. pyWannier90: A Python Interface for Wannier90. **2019**,

(58) Peschel, I.; Eisler, V. Reduced density matrices and entanglement entropy in free lattice models. *Journal of Physics A: Mathematical and Theoretical* **2009**, *42*, 504003.

(59) Pham, H. Q. pDMET: A Code for Periodic DMET Calculations. 2019; `https://github.com/hungpham2017/pDMET`, accessed Sep, 29, 2022.

(60) Mitra, A. pDMET: A Code for Periodic DMET Calculations. 2022; `https://github.com/mitra054/pDMET`, accessed November, 24, 2022.

(61) Sun, Q.; Berkelbach, T. C.; Blunt, N. S.; Booth, G. H.; Guo, S.; Li, Z.; Liu, J.; McClain, J. D.; Sayfutyarova, E. R.; Sharma, S.; Wouters, S.; Chan, G. K.-L. PySCF: the Python-based simulations of chemistry framework. *WIREs Computational Molecular Science 8*, e1340.

(62) Sun, Q. et al. Recent developments in the PySCF program package. *The Journal of Chemical Physics* **2020**, *153*, 024109.

(63) Goedecker, S.; Teter, M.; Hutter, J. Separable dual-space Gaussian pseudopotentials. *Phys. Rev. B* **1996**, *54*, 1703–1710.

(64) Andersson, K.; Malmqvist, P.; Roos, B. O. Second-order perturbation theory with a complete active space self-consistent field reference function. *The Journal of Chemical Physics* **1992**, *96*, 1218–1226.

(65) Goldman, M. L.; Doherty, M. W.; Sipahigil, A.; Yao, N. Y.; Bennett, S. D.; Manson, N. B.; Kubanek, A.; Lukin, M. D. Erratum: State-selective intersystem crossing in nitrogen-vacancy centers [Phys. Rev. B 91, 165201 (2015)]. *Phys. Rev. B* **2017**, *96*, 039905.

(66) Delaney, P.; Greer, J. C.; Larsson, J. A. Spin-Polarization Mechanisms of the Nitrogen-Vacancy Center in Diamond. *Nano Letters* **2010**, *10*, 610–614.

TOC Graphic

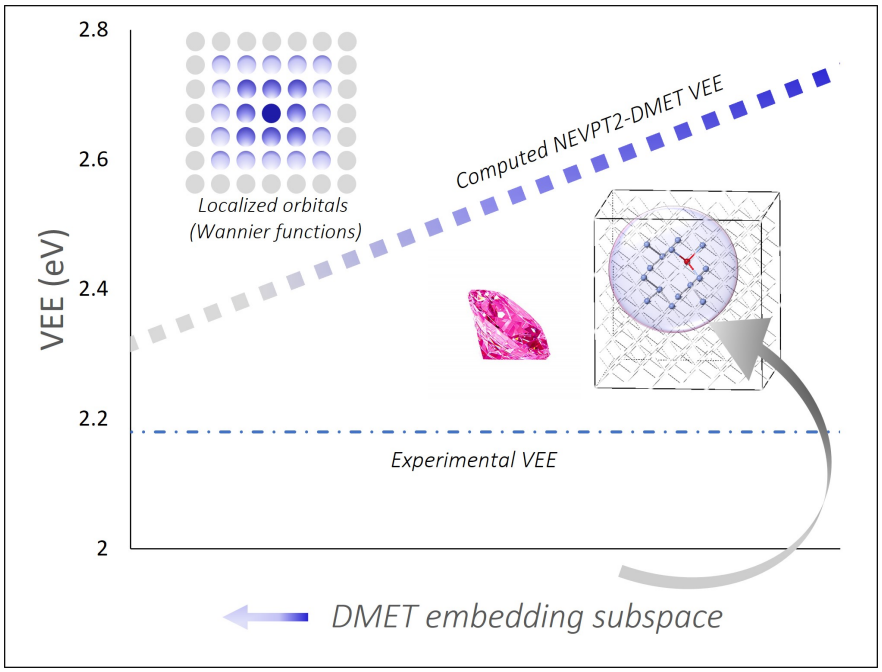

Figure 5: TOC